Pergamon

Acta mater. Vol. 45, No. 10, pp. 4131–4143, 1996
Elsevier Science Ltd

0956-7151/96 $15.00 + 0.00

PII: S1359-6454(97)00089-X

THE INFLUENCE OF INTERFACE AND ARRANGEMENT OF INCLUSIONS ON LOCAL STRESSES IN COMPOSITE MATERIALS

AHMED AL-OSTAZ[1] **and IWONA JASIUK**[2]

[1]Department of Materials Science and Mechanics, Michigan State University, East Lansing, MI 48824-1226, [2]The George W. Woodruff School of Mechanical Engineering, Georgia Institute of Technology, Atlanta, GA 30332-0405, U.S.A.

(Received 25 July 1996; accepted 14 February 1997)

Abstract—We studied a model composite material consisting of a thin epoxy plate (matrix) reinforced with stiff circular disks (inclusions) and subjected to a uniaxial tension. At each inclusion–matrix interface there is an interfacial layer, an interphase, which has uniform properties. The inclusions are arranged in the matrix at random but with no overlap. For comparison we also considered square and triangular periodic arrangements. We have studied elastic fields of such composites both experimentally, using a photoelasticity method, and numerically via a finite element method. We have found that random inclusion arrangements give higher stress concentrations than the periodic ones owing to stress localizations. The highest stress increase is in a compliant interface case, which also exhibits the highest scatter in stress magnitudes for different random arrangements at the same volume fraction. © *1997 Acta Metallurgica Inc.*

1. INTRODUCTION

A knowledge of local stresses in matrix–inclusion composite materials is important for design purposes since the presence of inclusions may give rise to stress concentrations, which, in turn, may result in initiation of cracking and/or plasticity. There are many factors which influence stress fields in composites: the mismatch in material constants, the shape and geometric arrangement of inclusions, the boundary conditions at inclusion–matrix interfaces, and the proximity to a surface. In this paper we focus on the joint influence of the geometric arrangement of inclusions and the matrix–inclusion interface on local elastic fields.

A fundamental problem in the evaluation of local stress fields is the single inclusion solution [1, 2], which is applicable for composites with inclusions placed far apart. When inclusions are closely spaced stress fields interact and solutions become very complex. In order to simplify this problem effective medium approaches, such as the Mori–Tanaka method, for example, based on a single inclusion solution, have been used in the analytical predictions of stress fields [3–5]. Numerical approaches usually involve the assumption that the arrangement of inclusions is periodic: square or hexagonal [6–10], or of more complex type [11, 12]. However, the distribution of fibers in composites is in general disordered. Thus, the above approaches may give good predictions for effective elastic and thermal constants, and average stresses, but they cannot capture local fields in composites with randomly arranged and interacting inclusions. A knowledge of local fields is needed in studies of damage initiation and propagation in composite materials since the damage, such as plasticity and fracture, is a localized phenomenon influenced by a geometric (and material) disorder [13–19].

The influence of a random arrangement of fibers on local fields and/or effective properties was studied numerically [15–25] and analytically [26, 27]; the more basic studies focusing on inclusion interactions involved solutions of two neighboring inclusions [28–30].

Experimentally, the local stress due to a cast-in-place single inclusion and inclusions in a periodic arrangement were studied, using a photoelasticity method, in Refs [31–35] among others.

Another important and complicating factor which influences the response of composites is the matrix–inclusion interface. The interface is often represented as a thin layer or a coating around the fiber and is called an *interphase* [36]. The interphase may be a result of a chemical reaction, diffusion, or of other complex processes which occur during processing. The influence of the interphase on local fields and effective properties of composites has been the subject of intensive studies in the last decade [e.g. 4–10, 37–40]; for reviews see Refs [41–43]. However, the joint effect of the geometric arrangement of inclusions and the inclusion–matrix interface has not yet been explored.

The objective of this paper is to study the local stress fields in a transverse plane of a unidirectional fiber-reinforced composite. However, for simplicity we focus on a model composite made of a thin sheet with an epoxy matrix and circular copper inclusions. At each matrix–inclusion interface there is an interfacial layer, which we refer to as the interphase or the coating. Inclusions are arranged randomly in the matrix but with the restriction that they are not allowed to overlap and that there is a minimum distance between them. For comparison we also include composites with triangular and square periodic arrangements. We subject these composites to a mechanical loading, the uniaxial tension, and analyze the local stress fields experimentally by using a photoelasticity method and numerically via a finite element method. We also consider a single coated inclusion problem, which we solve analytically, numerically and experimentally, as well as other simple geometries.

We study a model composite in the form of a thin plate in order to simplify the experimental analysis. By having the plane stress case we reduce free edge effects, i.e. a disturbance of stresses near traction-free surfaces owing to a relaxation of stresses there, and in this case, we can see photoelastic fringes more easily. Alternately, we could simulate a three-dimensional case directly by using a stress freezing technique [34].

This paper extends our earlier preliminary study involving finite element and photoelastic analyses of a sheet with randomly arranged coated disks [44]; our related work is given in Ref. [45]; for more details see Ref. [46].

2. THE SINGLE INCLUSION SOLUTION

A fundamental problem in micromechanics is one involving a single inclusion in an infinite matrix. The famous result dealing with a single inclusion is due to Eshelby [1], who found that the stress field in an ellipsoidal and perfectly bonded inclusion, subjected to either a uniform transformation strain or a uniform remote traction, is constant. The solution of a single inclusion is applicable for the dilute case, in which inclusions are far away from each other and do not interact, but it also gives a basic understanding of the stress fields in composite materials in general.

Thus, we first briefly consider a single coated inclusion solution and discuss the influence of several parameters on the local stress fields. In the analysis we assume that all components of the composite are linearly elastic and isotropic. We denote Young's modulus and Poisson's ratio of the constituents by E and v, and use the superscripts i, c, and m to refer to the inclusion, coating (interphase), and matrix, respectively. The geometry involves a large plate containing a small circular inclusion of radius a with the interphase of thickness t. Thus, we have an elasticity problem of plane stress type. The applied loading is a remote uniaxial tension. In the analysis it is convenient to employ the polar coordinate system (r, θ). We assume perfect bonding conditions, which imply a continuity of tractions and displacements at the inclusion–coating $(r = a)$ and the coating–matrix $(r = a + t)$ interfaces.

For an applied uniaxial tension, $\sigma_{yy} = \sigma_0$, at infinity, our plane elasticity problem can be solved by using the following Airy stress functions Φ [e.g. 47]:

$$\Phi^{m} = \frac{\sigma_0}{4}\left(r^2 + r^2\cos 2\theta + A\log r + \frac{B\cos 2\theta}{r^2} + C\cos 2\theta\right) \tag{1}$$

$$\Phi^{i} = \frac{\sigma_0}{4}\left(Dr^2 + Fr^2\cos 2\theta + Gr^4\cos 2\theta\right) \tag{2}$$

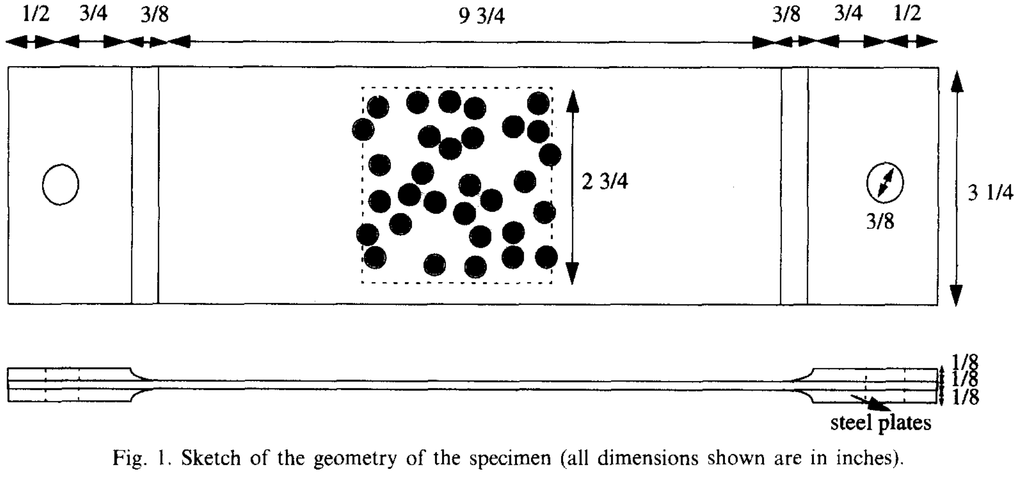

Fig. 1. Sketch of the geometry of the specimen (all dimensions shown are in inches).

$$\Phi^c = \frac{\sigma_0}{4}\left(Hr^2 + J\log r + L\frac{\cos 2\theta}{r^2} + M\cos 2\theta + Nr^2\cos 2\theta + Qr^4\cos 2\theta\right) \quad (3)$$

where A, B, C, D, F, G, H, J, L, M, N, and Q are constants which are evaluated using boundary conditions. The results of a parametric study are shown in Figs 2 and 3 and Table 3.

If the initiation of plasticity were of interest, then it is convenient to use an equivalent or effective stress σ_{eff}, based on the Huber–von Mises yield criterion [e.g. 48], and defined as

$$\sigma_{eff} = \frac{1}{\sqrt{2}}[(\sigma_{rr} - \sigma_{\theta\theta})^2 + (\sigma_{zz} - \sigma_{\theta\theta})^2 + (\sigma_{rr} - \sigma_{zz})^2 + 6(\sigma_{r\theta}^2 + \sigma_{\theta z}^2 + \sigma_{rz}^2)]^{1/2} \quad (4)$$

where for the plane stress case, considered in this paper, $\sigma_{zz} = \sigma_{\theta z} = \sigma_{rz} = 0$.

3. THE MULTI-INCLUSION SOLUTION

When many inclusions are present in a material and they are closely spaced, the problem of finding local stresses becomes very complex owing to the inclusions' interactions. The analytical solution for a problem of multiple coated inclusions is possible, in principle, by using the approach of Gong and Meguid [26] or Honein *et al.* [27], for example, but it would be very involved. Alternately, numerical means, such as finite element, boundary element, and finite difference methods, or experimental approaches, such as optical methods, can be used. In this paper, for simplicity, we use the finite element program ANSYS [49] and the photoelasticity method [e.g. 50] to predict elastic fields in a composite with randomly arranged inclusions. For comparison we consider composites with square and triangular periodic arrangements of inclusions, too. Also, we use these two methods to find solutions for a single inclusion problem and compare them with the analytical solution, discussed in Section 2, in order to check the accuracy of our experimental and numerical approaches.

3.1. *The experimental approach (photoelasticity)*

The experimental set-up involved thin epoxy plates (PSM-5), with dimensions of 82.6 mm × 330 mm × 3.2 mm ($3\frac{1}{4}$ in × 13 in × $\frac{1}{8}$ in), containing over thirty (31) randomly distributed but non-overlapping coated circular copper inclusions with 6.4 mm ($\frac{1}{4}$ in) diameters. To create a non-uniform arrangement of inclusions, random numbers, indicating centers of inclusions, were generated on a computer according to a planar Poisson's distribution. We imposed restrictions that the inclusions didn't overlap, were located at least one inclusion diameter away from an edge of a specimen [51], and there was a minimum clear distance of one tenth of an inclusion radius a ($0.1a$) between any two inclusions. All the inclusions were placed in the middle portion of the specimen 69.8 mm × 79.4 mm ($2\frac{3}{4}$ in × $3\frac{1}{8}$ in) (a volume fraction of inclusions was approximately 23% in that region) leaving both ends of the specimen inclusion free. This way we had one-width long regions of a homogeneous material between gripped sides of the specimen and the inclusions region. A sketch of a sample specimen with dimensions is shown in Fig. 1.

Table 1. Elastic properties of the matrix, inclusions, and coatings used in the experimental analysis

Material	ν	E (ksi)	E (MPa)	E/E^m
Coating 1	0.4	1	7	0.002
Coating 2	0.4	30	207	0.067
Matrix	0.36	450	3102	1
Inclusions	0.34	17,400	119,963	38.667

The specimens were prepared in the following way. First, the epoxy plates were cut to the desired dimensions. Then they were placed one at a time between two steel plates and holes were drilled at a slow speed to reduce residual stresses and to minimize microcracks. The holes were of a diameter equal to the combined size of an inclusion and a coating (7.9 mm — $\frac{5}{16}$ in) or to the size of an inclusion (6.4 mm — $\frac{1}{4}$ in) for a two-phase composite. To remove any remaining residual stresses owing to machining, the specimens were heated to 127°C (260°F) (which is beyond the glass transition temperature), were held at this temperature for 2 h, cooled at a rate of 2.8°C/h (5°F/h) to 66°C (150°F), and then cooled in 7 h to room temperature. To simulate different interphases, copper inclusions were coated with two different adhesive materials, PC-1 (coating 1) and PC-6 (coating 2), which were more compliant than the matrix, while an adhesive PC-11 was used for a two-phase case (i.e. the no-coating case or, equivalently, the case where the coating has the same properties as the matrix, i.e. $E^c = E^m$). This was done by placing inclusions in the holes and filling the remaining spaces with the adhesives, which also served as gluing agents between copper inclusions and epoxy matrix. The adhesives underwent setting at room temperature and thus no residual stresses resulted in this process. Elastic properties of these materials are given in Table 1.

After the preparation of samples the photoelasticity method was used to find stress distributions in these birefringent composite plates. The specimens were loaded uniaxially to $p = 3.39$ MPa (492 psi) using a screw type testing machine (this loading corresponded to an applied force of 100 lb). They were gripped approximately one width away from the inclusions region on both sides. The loading was applied as follows: one side remained stationary (fixed grip) while the other was subjected to a traction-controlled uniaxial load; the remaining two sides were traction free. This loading was small enough not to cause any permanent damage in the

Table 2. Elastic properties of coatings used in the numerical analysis

Coating	E^c (ksi)	E^c (MPa)	E^c/E^m	ν^c	Description
1	1	7	0.002	0.36	Very compliant
2	30	207	0.067	0.36	Compliant
3	120	827	0.267	0.36	Optimum
4	450	3102	1	0.36	$E^c = E^m$
5	9000	62,050	20	0.36	Stiff $E^c = (E^m + E^i)/2$
6	90,000	620,500	200	0.36	Very stiff

specimens but at the same time allowed us to see several fringe orders. Owing to the absence of residual stresses we were able to isolate the contribution of the mechanical loading only. The effects of residual stresses were studied elsewhere [46]. In order to calibrate epoxy for a material fringe value f_σ, the load increments were applied to either specimens with a hole or to a four-point-loaded beam. The average value of a number of fringes was used to determine f_σ according to the formula $\sigma_1 - \sigma_2 = Nf_\sigma/h$, where h is the specimen thickness, N is the fringe order, and σ_k, $k = 1$, 2, are principal in-plane normal stresses ($\sigma_1 - \sigma_2$ is twice the magnitude of a maximum in-plane shear stress). For our case f_σ was found to be 9281 N/m (53 lb/in).

3.2. The finite element solution

In the numerical study we used the commercially available finite element package ANSYS 5.1 [49]. We utilized quadrilateral plane elements, such that each element was defined by eight nodes having two degrees of freedom: translations in the nodal x- and y-directions. We specified the element edges to be $0.4a$ along the interfaces of inclusions and $1.6a$ along the outer edges of the region of observation (shown in Figs 4–5). Then, the elements were generated automatically using ANSYS. In this numerical analysis, we simulated the exact geometry of the experimental specimens, described in the previous section, with the following boundary conditions: traction-free conditions at two parallel side edges (top and bottom in Fig. 1), an applied uniaxial tension at the third edge (right side in Fig. 1), and a fixed displacement condition at the remaining edge (left side in Fig. 1). Numerically, we used six different coatings (Table 2), ranging from very compliant to very stiff, and considered seven different random arrangements of inclusions while keeping the volume fraction of inclusions fixed. Other studied geometries included square and triangular periodic arrangements, and two, three, and four inclusion cases.

4. RESULTS AND DISCUSSION

4.1. The single inclusion case

In the parametric study of a single coated inclusion solution, obtained analytically and discussed in Section 2, we illustrate the influence of three parameters characterizing the coating (interphase): Young's modulus E^c, Poisson's ratio ν^c, and the thickness t, on the elastic stress fields. The composite system is a thin epoxy plate with copper inclusions with properties given in Table 1 and the loading is the uniaxial tension $\sigma_{yy} = \sigma_0$.

Figure 2(a), (b) shows the joint effect of the non-dimensionalized Young's modulus of the coating, E^c, with respect to the Young's modulus of the matrix E^m (E^c/E^m) and the non-dimensionalized thickness t with respect to the inclusion radius a (t/a) on the radial stress σ_{rr}^m at $\theta = \pi/2$ and the hoop stress $\sigma_{\theta\theta}^m$ at $\theta = 0$, respectively, at $r = a + t$ when $\nu^c = 0.36$; θ is the angle taken from the x-axis. Observe that both the thickness t and the Young's modulus of the coating E^c influence stress fields. The effect of E^c on the stresses in the matrix is more pronounced when the coating is very compliant, i.e. E^c/E^m is small. Thus, we only plot the results in the range $0 \leqslant E^c/E^m \leqslant 1$. It is interesting to observe that this effect of E^c is higher on $\sigma_{\theta\theta}^m$ at $\theta = 0$ when the

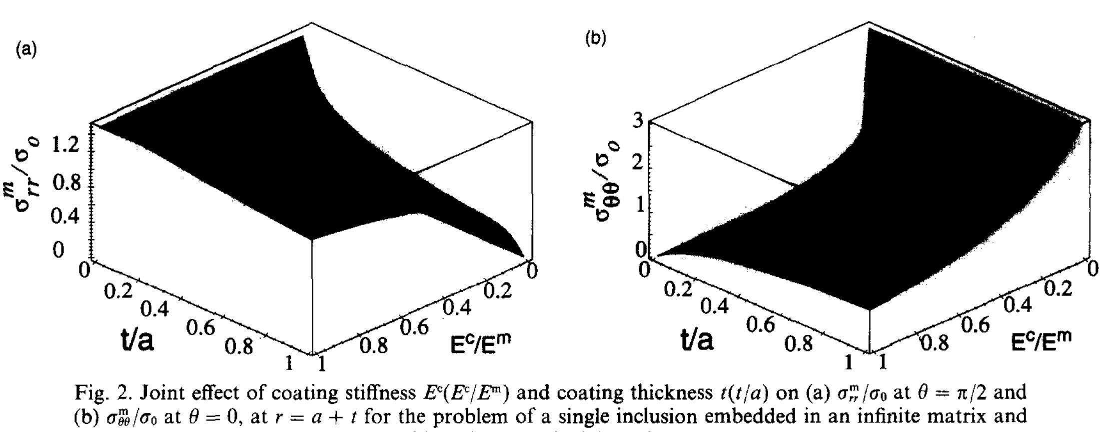

Fig. 2. Joint effect of coating stiffness $E^c(E^c/E^m)$ and coating thickness $t(t/a)$ on (a) σ_{rr}^m/σ_0 at $\theta = \pi/2$ and (b) $\sigma_{\theta\theta}^m/\sigma_0$ at $\theta = 0$, at $r = a + t$ for the problem of a single inclusion embedded in an infinite matrix and subjected to a uniaxial tension σ_0.

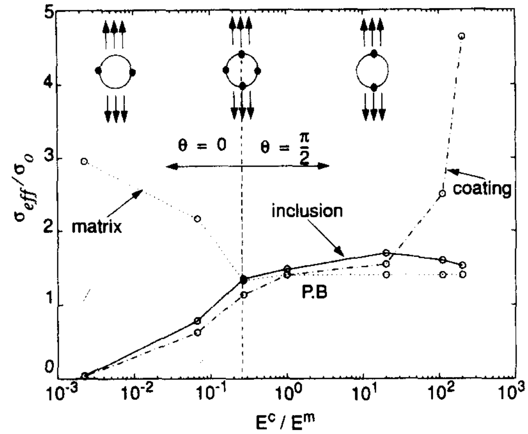

Fig. 3. Influence of coating stiffness E^c on σ_{eff}/σ_0 of the matrix, coating and inclusion at $r = a + t = 1.25a$ for a single inclusion case under a uniaxial tension σ_0.

thickness is very small while the opposite behavior is true for σ^m_{rr} at $\theta = \pi/2$.

The effect of the Poisson's ratio of the coating material, ν^c, is very small in comparison to the influence of the other two parameters, E^c and t, as shown in Fig. 2.3(c), (d) in Ref. [46]. Thus, in our finite element calculations we assume a common value of $\nu^c = 0.36$ for all six coatings studied. Also, in all the remaining numerical and experimental examples in this paper we take $t = a/4$.

Figure 3 illustrates the maximum effective stress σ_{eff}/σ_0 in the matrix, inclusion, and coating (dotted, solid, and dash–dot lines, respectively) as a function of E^c/E^m for the single inclusion case. Note that for the case of a compliant coating the maximum stress in the matrix is in a plane perpendicular to the applied loading ($\sigma^m_{\theta\theta}$ at $\theta = 0$), while for the case of a stiff coating the maximum stress is located along the line of action of the applied load (σ^m_{rr} at $\theta = \pi/2$) as shown in the sketches. Carman *et al.* [52] observed that when the hoop stress at $\theta = 0$ and the radial stress at $\theta = \pi/2$ are equal, then the stress concentration in the matrix is minimum. They refer to such a situation as the "optimum interphase" case with respect to stresses. For our model composite material the elastic modulus of such an optimum coating is $E^c = 827$ MPa (120 ksi) (denoted as coating 3 in Table 2). In the case of a very compliant coating, $E^c/E^m \ll 1$, the maximum effective stress is located in the matrix, and the inclusion and coating carry almost no load, although the inclusion is much stiffer (since there is almost no load transfer across the interface). As the value of E^c increases, both the coating and the inclusion start carrying the load. In the case of a very stiff coating, $E^c/E^m \gg 1$, the maximum stress in the composite is located in the coating. Note that when $E^c/E^m > 1$ and the inclusion is stiff, the stress field in the matrix remains nearly unchanged, as seen in Fig. 3.

Table 3 summarizes magnitudes and locations of the maximum stresses σ_{eff}/σ_0 and $(\sigma_1 - \sigma_2)/\sigma_0$ in different constituents of the composite (matrix, coating, and inclusion). Note that the locations of the maximum stress are not necessarily at one of the interfaces. The maximum stress in the matrix is at the coating–matrix interface for a compliant coating case but as the coating stiffness increases the locations of the maximum stress move further away from the interface. The locations of the maximum stresses in the coating also vary with the radial coordinate and depend on E^c and the angle. Stresses in the coated inclusion are uniform, as expected from the solution of Eshelby [1].

Table 3. Magnitudes and locations of maximum stresses σ_{eff}/σ_0 and $(\sigma_1 - \sigma_2)/\sigma_0$ in a single inclusion case under a uniaxial tension σ_0, obtained analytically ($t = a/4$)

	Coating						
Stress	1	2	3	4	5	6	Angle
Matrix							
σ_{eff}/σ_0	0.995	1.07	1.33	1.40	1.40	1.40	0°
	$r = 1.25a$	$r = 1.25a$	$r = 1.25a$	$r = 1.267a$	$r = 1.57a$	$r = 1.60a$	
$(\sigma_1 - \sigma_2)/\sigma_0$	1.01	1.25	1.41	1.35	1.35	1.35	
	$r = 1.25a$	$r = 1.25a$	$r = 1.25a$	$r = 1.43a$	$r = 1.73a$	$r = 1.77a$	
σ_{eff}/σ_0	2.96	2.17	1.33	1.00	1.00	1.00	90°
	$r = 1.25a$	$r = 1.25a$	$r = 1.25a$	$r \to \infty$	$r \to \infty$	$r \to \infty$	
$(\sigma_1 - \sigma_2)/\sigma_0$	2.96	2.25	1.45	1.00	1.00	1.00	
	$r = 1.25a$	$r = 1.25a$	$r = 1.25a$	$r \to \infty$	$r \to \infty$	$r \to \infty$	
Coating							
σ_{eff}/σ_0	0.034	0.624	1.13	1.40	1.55	1.85	0°
	$r = 1.06a$	$r = 1.07a$	$r = 1.125a$	$r = 1.25a$	$r = 1.25a$	$r = a$	
$(\sigma_1 - \sigma_2)/\sigma_0$	0.254	0.496	0.955	1.32	1.61	2.10	
	$r = 1.06a$	$r = 1.15a$	$r = 1.22a$	$r = 1.25a$	$r = 1.25a$	$r = a$	
σ_{eff}/σ_0	0.012	0.227	0.434	0.663	1.30	4.64	90°
	$r = 1.25a$	$r = 1.25a$	$r = 1.25a$	$r = 1.25a$	$r = 1.25a$	$r = a$	
$(\sigma_1 - \sigma_2)/\sigma_0$	0.014	0.256	0.503	0.736	1.31	4.81	
	$r = 1.25a$	$r = 1.25a$	$r = 1.25a$	$r = 1.25a$	$r = 1.25a$	at $r = a$	
Inclusion							
σ_{eff}/σ_0	0.043	0.782	1.35	1.49	1.69	1.52	0–90°
						$0 \leqslant r \leqslant a$	
$(\sigma_1 - \sigma_2)/\sigma_0$	0.047	0.844	1.42	1.50	1.66	1.67	
						$0 \leqslant r \leqslant a$	

We also studied a single inclusion problem experimentally, using the photoelasticity method. In the case of a two-phase composite (matrix and inclusion only) fringes start forming at the inclusion–matrix interface along the line of action of the applied load and then they propagate to the sides of the inclusion (Fig. 7 in Ref. [44] or Fig. 2.5 in Ref. [46]). The opposite behavior is observed in the cases of an inclusion with a compliant coating (Fig. 8 in Ref. [44] or Fig. 2.6 in Ref. [46]) or a hole, in which fringes start forming in a plane perpendicular to the line of action of the applied load and eventually migrate to the line parallel to the line of action of the applied load.

4.2. *The multi-inclusion case*

The case of a composite with a 23% volume fraction of randomly distributed inclusions [Fig. 4(a), (b)] shows similar behavior, in terms of the fringe pattern formation, to that observed for the single inclusion case, discussed in the previous section and illustrated in Figs 7 and 8 in Ref. [44]. Recall that fringe patterns denote contours of a difference in normal in-plane principal stresses, $\sigma_1 - \sigma_2$, or a maximum in-plane shear stress, $\tau_{max} = (\sigma_1 - \sigma_2)/2$. Figure 4(a) gives fringe patterns in the matrix of a two-phase composite and Fig. 4(b) in the matrix of a composite with a very compliant interphase (coating 1) for the same inclusion arrangement and the same load of $\sigma_0 = 3.39$ MPa (492 psi), applied in the horizontal direction. Note that non-transmissible regions are those of the inclusions in Fig. 4(a) and of the inclusions and the coatings in Fig. 4(b). Also, in Fig. 4 only the close-ups of inclusion regions are shown in order to give a better resolution of details. The numbers in Fig. 4 denote fringe numbers and the higher the number, the higher the maximum shear stress [e.g. 50]. Observe that stress fields in the matrix are very non-uniformly distributed in both cases and the stresses in the matrix are much higher in the compliant interphase case [Fig. 4(b)], as expected from the parametric study of a single inclusion case (see Table 3).

In Fig. 5(a), (b) the finite element outputs illustrate the joint effect of the random arrangement and interface on σ_{eff} for the same geometric arrangement of fibers and the corresponding properties as in Fig. 4(a), (b), for a uniaxial horizontal tension; again, only the middle portion of the specimen is shown. Note that color scales are different in Fig. 5(a) and (b). This way the trends are clearer for each case individually. The use of the same scale would result in only blue shades for a perfectly bonded case. Our finite element calculations also include four additional interphase cases given in Table 2. Stress contours for those cases are shown in Fig. 2.10(c)–(f) in Ref. [46].

We observe that when the interface is very compliant (coating 1), then almost no load is transferred from the matrix to the inclusions and it is carried by the matrix [Fig. 5(b)]. When the interface is compliant (coating 2), but yet capable of transferring some loads to the inclusions, then the loads are carried in part by the coatings and inclusions, but the maximum stress still occurs in the matrix. In the case of an optimum coating (minimum stress condition) the load is shared more equally between the matrix, coating and inclusions. If the interphase elastic modulus E^c increases further and a good bond is maintained between interfaces then the load is carried mainly by the stiff inclusions [Fig. 5(a)] and the coatings. But if the coating is very stiff then the highest stress occurs in the coating. Note that this behavior for the multi-inclusion case discussed here is similar to the one observed for a single inclusion case and illustrated in Fig. 3.

In Fig. 5(a) there is bridging of stresses through the inclusions along the line of action of the applied load. The inclusions close to each other and aligned in the direction of the load behave like longitudinal fibers subjected to an axial loading. For inclusions with a compliant interphase, shown in Fig. 5(b), the maximum stress around each inclusion is located in a plane perpendicular to the applied loading, as we observed in the single inclusion case. Similar behavior occurs in elastic sheets with holes.

Also, Fig. 5(a) shows that the load is distributed very unevenly between the inclusions. This is in contrast to periodic arrangements in which inclusions share loads equally. In Fig. 5(b) we see a localization of stresses in the matrix. In the periodic arrangements the stress field is distributed throughout the composite and is lower in magnitude as shown in Table 4 (note that out of the two periodic cases considered the triangular arrangement gives lower stresses than the square one for the same volume fraction). Thus, the non-uniform arrangement leads to the stress localization and higher maximum stresses and, hence, to an earlier initiation of damage and consequently a lower strength. These issues were also discussed elsewhere [e.g. 15, 18, 19].

Table 4 summarizes the results for the maximum effective stress σ_{eff} in the matrix, coating, and inclusions for seven random arrangements and two periodic arrangements (square, with a uniaxial traction applied along the rows, and triangular). The volume fraction used in these calculations is 23% for both random and periodic arrangements. We also include the results for two isolated inclusions, embedded in an epoxy matrix or in an effective medium. These pairs of inclusions were chosen from each of the above seven arrangements because they had the maximum stress in the matrix in their vicinity in the multi-inclusion configuration. In other words we removed the other 29 inclusions from the seven 31-inclusion configurations (i.e. replaced them by either matrix or effective medium) keeping the identical mesh as in the random arrangement. The effective medium properties were calculated by using the Mori–Tanaka method [4]. We observe that for the

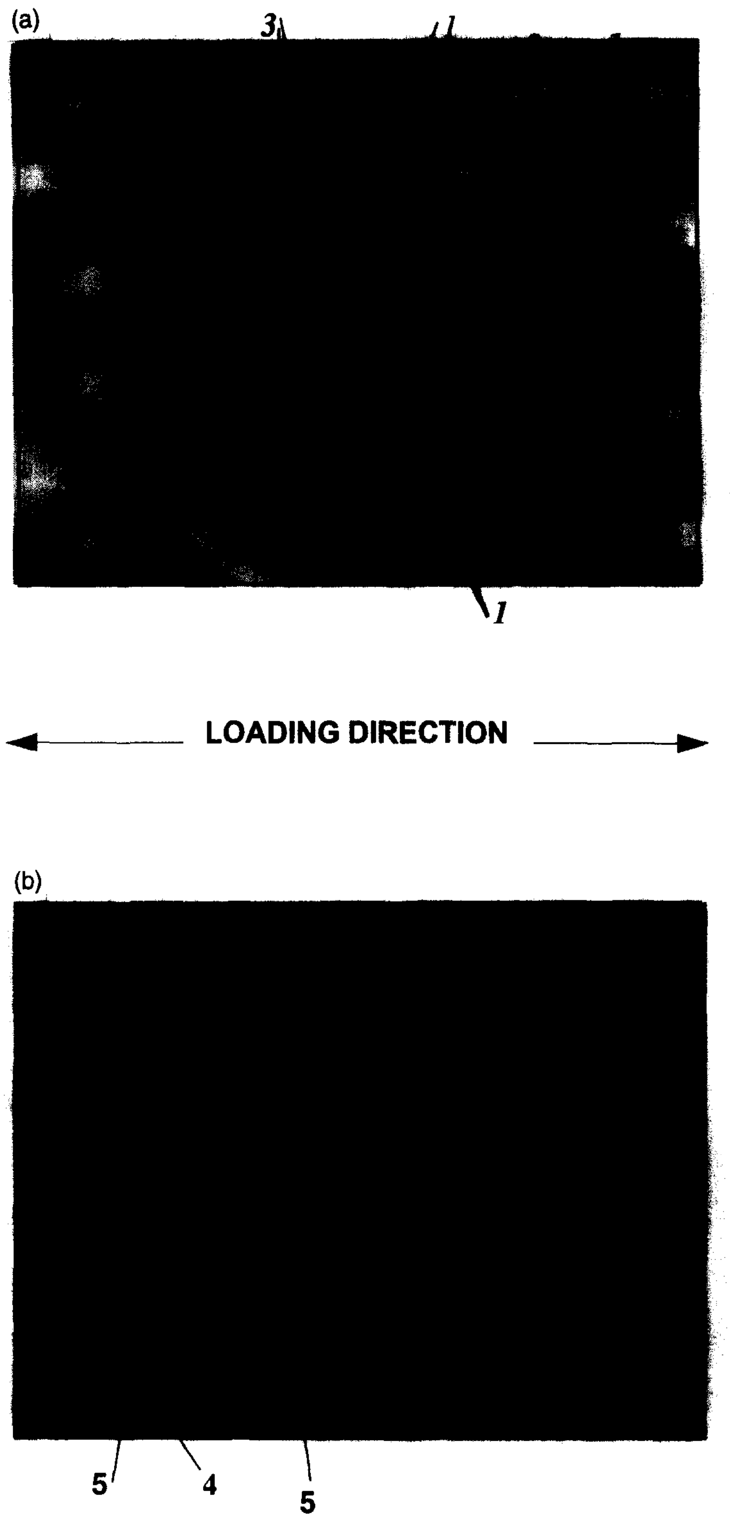

Fig. 4. Isochromatic fringe patterns in an epoxy matrix with randomly distributed copper inclusions for a uniaxial applied stress of $\sigma_0 = 3.39$ MPa in the horizontal direction for (a) the two-phase composite ($E^c/E^m = 1$) and (b) the coating 1 case ($E^c/E^m = 1/450$) when $t = a/4$ and $f = 23\%$.

compliant coating cases the two inclusions embedded in either the matrix or the effective medium give a lower effective stress than the one in the actual composite, and the stresses are higher near the two inclusions placed in the matrix than in the effective medium, as expected, because of a higher mismatch in elastic moduli. The opposite behavior is observed for the stiff coating cases. The maximum effective stress values, found in Table 4, are averaged (denoted by AVG) based on seven configurations. Thus, the inclusion pair is not sufficient to give estimates of the maximum stress fields in the multi-inclusion environment and the neighboring inclusions have an important contribution to these stress fields.

For all geometries, the effective stresses in the matrix are highest when the interphase is most compliant. This is expected, since, in this case, the matrix carried most of the load, although the inclusions are much stiffer than the matrix material. Another important observation is that there is a very

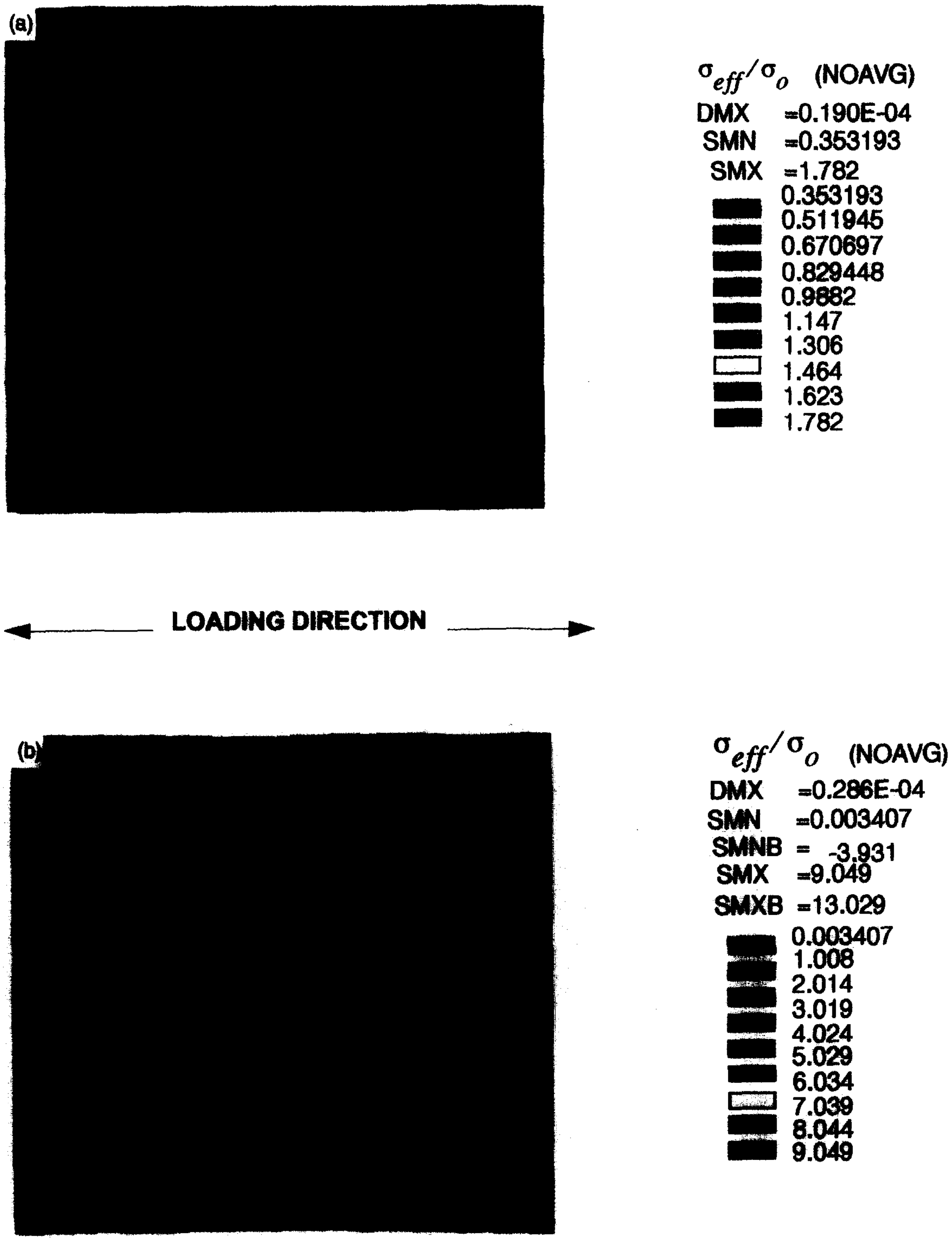

Fig. 5. The stress $\sigma^{m}_{eff}/\sigma_0$ in a model composite with randomly distributed inclusions, subjected to a uniaxial tension σ_0 in the horizontal direction, obtained by FEM for (a) the two-phase composite ($E^c/E^m = 1$) and (b) the coating 1 case ($E^c/E^m = 1/450$) when $t = a/4$ and $f = 23\%$.

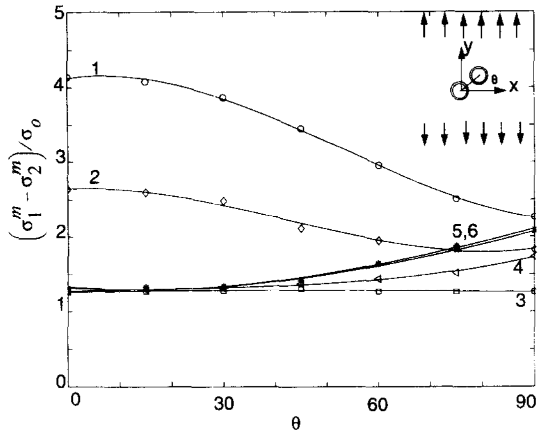

Fig. 6. Effect of inclination angle θ on the normal in-plane principal stress difference $(\sigma_1^m - \sigma_2^m)/\sigma_0$ in the matrix for the two inclusion case when $t = a/4$.

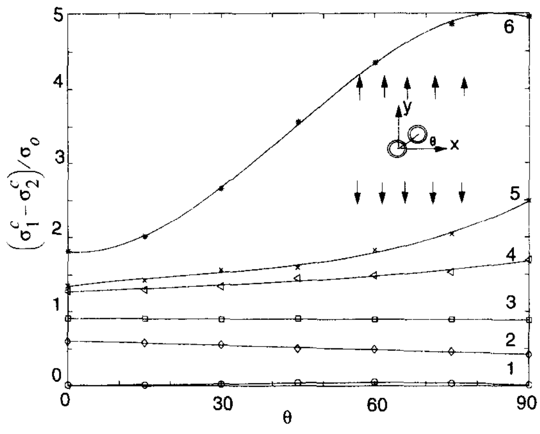

Fig. 7. Effect of inclination angle θ on $(\sigma_1^c - \sigma_2^c)/\sigma_0$ for the two inclusion case ($t = a/4$).

large scatter in data (standard deviation, denoted as STD in Table 4) for compliant coating cases and it decreases considerably as the coating stiffness increases.

4.3. *The two-inclusion solution*

In order to gain insight about the interaction of stress fields in a multi-inclusion configuration we focused also on the two-inclusion solution. The local stress fields owing to two inclusions depend on an inclination angle between the two inclusions with respect to an applied loading, a separation distance between the two inclusions, and the presence of other inclusions. We define the angle of inclination θ_{inc} as the angle between a line connecting centers of two inclusions and a line perpendicular to the applied uniaxial loading. We conducted this study numerically. In the analysis we placed the two inclusions in a matrix of dimensions $3a \times 5a$. We used a fine mesh with element edges of $0.1a$ along interfaces and applied a remote unit uniaxial tension. We kept the same type of mesh for all geometries, i.e. did not refine the mesh as the inclusions approached each other. We followed this approach for computational simplicity. Also, in this paper our objective was to report the trends rather than to focus on high numerical accuracy.

4.3.1. Effect of the inclination angle on local elastic stress fields. First, we explore the effect of the angle of inclination θ_{inc}. We consider numerically the case of two coated inclusions separated by a constant distance $d = a$ and inclined by the angle $\theta_{inc} = \theta$. The influence of the inclination angle on the maximum in-plane principal normal stress difference $\sigma_1 - \sigma_2$ (or the maximum in-plane principal shear stress) in the matrix and coating is shown in Figs 6 and 7, respectively. The location of the maximum stress difference $\sigma_1^m - \sigma_2^m$ is at $\theta = 0$, i.e. when the two

Table 4.

Arrangement		Coating 1	2	3	4	5	6	
Periodic (square)		3.38	2.29	1.42	2.03	2.47	2.52	Matrix
Periodic (triangular)		3.10	1.81	1.15	1.32	2.02	2.09	
Random	AVG	⟨8.17⟩	⟨4.07⟩	⟨1.51⟩	⟨2.41⟩	⟨3.09⟩	⟨2.98⟩	
	STD	2.45	1.461	0.101	0.112	0.113	0.113	
Two inc. in matrix	AVG	⟨5.20⟩	⟨3.51⟩	⟨1.50⟩	⟨2.50⟩	⟨3.20⟩	⟨3.19⟩	
	STD	2.25	1.352	0.161	0.164	0.165	0.168	
Two inc. in eff. med.	AVG	⟨5.19⟩	⟨3.43⟩	⟨1.46⟩	⟨2.53⟩	⟨3.25⟩	⟨3.25⟩	
	STD	2.04	1.33	0.157	0.160	0.162	0.165	
Periodic (square)		0.003	0.534	1.24	2.13	2.40	4.07	Coating
Periodic (triangular)		0.002	0.426	1.20	1.44	2.31	3.86	
Random	AVG	⟨0.034⟩	⟨0.701⟩	⟨1.30⟩	⟨2.37⟩	⟨3.10⟩	⟨6.26⟩	
	STD	0.007	0.068	0.104	0.113	1.541	2.32	
Two inc. in matrix	AVG	⟨0.020⟩	⟨0.65⟩	⟨1.30⟩	⟨2.40⟩	⟨3.34⟩	⟨6.68⟩	
	STD	0.007	0.054	0.055	0.063	1.523	2.24	
Two inc. in eff. med.	AVG	⟨0.011⟩	⟨0.643⟩	⟨1.29⟩	⟨2.38⟩	⟨3.30⟩	⟨6.43⟩	
	STD	0.006	0.052	0.054	0.060	1.510	2.21	
Periodic (square)		0.009	0.693	1.39	2.11	3.40	3.14	Inclusion
Periodic (triangular)		0.001	0.599	1.26	1.58	2.80	2.62	
Random	AVG	⟨0.044⟩	⟨0.745⟩	⟨1.46⟩	⟨2.50⟩	⟨4.78⟩	⟨4.11⟩	
	STD	0.005	0.063	0.089	0.115	1.12	1.01	
Two inc. in matrix	AVG	⟨0.018⟩	⟨0.601⟩	⟨1.46⟩	⟨2.30⟩	⟨5.19⟩	⟨4.65⟩	
	STD	0.004	0.052	0.061	0.065	1.10	0.981	
Two inc. in eff. med.	AVG	⟨0.015⟩	⟨0.532⟩	⟨1.46⟩	⟨2.25⟩	⟨5.10⟩	⟨4.59⟩	
	STD	0.004	0.049	0.054	0.062	0.995	0.976	

inclusions are aligned in a plane perpendicular to the applied loading, for cases of compliant coating. In stiffer coating cases, the location of the maximum $\sigma_1^m - \sigma_2^m$ is at $\theta = \pi/2$, i.e. when the two inclusions are aligned along the line of action of the applied loading, as in the single inclusion solution discussed before. In the optimum coating case (coating 3), the stress in the matrix is almost the same for any angle of inclination of the two inclusions and is lowest for this case as expected. We can thus define two extreme angles of inclination: critical and optimum. We denote the critical angle of inclination as the angle which will produce the maximum stress. The optimum angle inclination is the angle that gives the minimum stress. We are interested in the critical angle, which for the soft coatings is at $\theta = 0$ and for the stiff coatings is at $\theta = \pi/2$.

The maximum in-plane shear stress in the coating is in the stiffest coating (coating 6) at $\theta = \pi/2$, while in the optimum coating case (coating 3) the stress is independent of θ, as shown in Fig. 7. The lowest stress in the coating is in the most compliant coating as expected.

Also, we found that the maximum shear stress in the inclusion has a small dependence on θ.

We compared results of our numerical calculations for a very compliant coating (hole) and for a perfect bonding case with the analytical solution of Kouris [30] when $d = a$ and $\theta = 0$, $\pi/2$ and found very good agreement between our finite element and his analytical results [46].

4.3.2. Effect of the separation distance between two inclusions. Next we vary the separation distance between the two coated inclusions inclined at either $\theta = 0$ or $\theta = \pi/2$. Figure 8 shows the maximum effective stress in the matrix σ_{eff}^m as a function of the separation distance between the two coated inclusions when the inclusions are placed at $\theta = 0$, i.e. along the line perpendicular to the uniaxial applied load. Note that decreasing the separation distance either increases or does not affect the local effective stress in the matrix. The stress in the matrix is highest when the coating is most compliant and the distance between the inclusions is very small (a limiting case of two nearby cavities was studied in Refs [53, 54], where the nature of stress singularity as holes nearly touched was examined). A similar but less pronounced behavior is observed for coating 2. When the elastic modulus of the coating is greater or equal to the modulus of the matrix ($E^c/E^m \geq 1$), the stress is unaffected by the distance between the inclusions. This is due to the fact that when the coating is compliant the maximum (hoop) stress occurs at the line perpendicular to the applied load ($\theta = 0$). Placing the second inclusion along that line increases the stress concentration. However, when the inclusion with the stiff coating is subjected to a uniaxial applied load the maximum (radial) stress is at $\theta = \pi/2$. In this case, placing the second inclusion along $\theta = 0$ does not influence the magnitude of the stresses. The opposite is true, however, when the inclusions are aligned along the line of loading ($\theta = \pi/2$) as shown in Fig. 9. In this situation, placing the second inclusion has no influence on stresses in the matrix when the inclusions have compliant coatings. However, it has a pronounced effect when $E^c/E^m \geq 1$. In this case stresses increase significantly as the distance between the two inclusions decreases. It is interesting to observe that there is a cross-over point, i.e. that at a larger separation distance the stresses are higher in the case of a compliant coating than in the case of a stiff coating.

4.3.3. Effect of the presence of other inclusions. Finally, we explore the effect of more than two inclusions on the stress field. We do so by considering three and four inclusions in a row aligned along a line perpendicular or parallel to the line of loading, which corresponds to the angles $\theta = 0$ (Fig. 10) and $\theta = \pi/2$

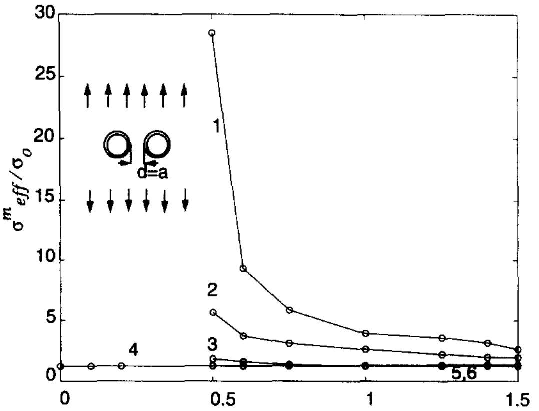

Fig. 8. Effect of separation distance d between two inclusions on the effective stress in the matrix $\sigma_{\text{eff}}^m/\sigma_0$ for a uniaxial tension σ_0 in the vertical direction when $t = a/4$ and $\theta = 0$.

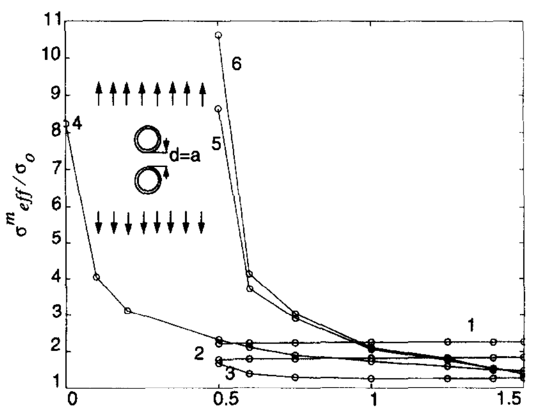

Fig. 9. Effect of separation distance d between two inclusions on the effective stress in the matrix $\sigma_{\text{eff}}^m/\sigma_0$ for a uniaxial tension σ_0 in the vertical direction when $t = a/4$ and $\theta = \pi/2$.

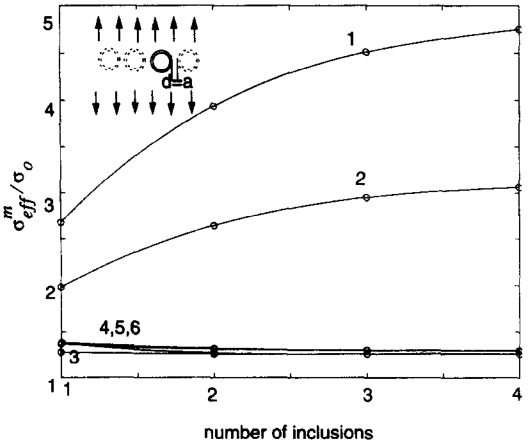

Fig. 10. Effect of number of inclusions on $\sigma^{m}_{eff}/\sigma_0$ for a uniaxial tension σ_0 in the vertical direction when $t = a/4$ and $\theta = 0$.

(Fig. 11), respectively, and three or four inclusions with their centers forming an equilateral triangle or a square.

Effect of Inclusions Aligned Along $\theta = 0$ and $\theta = \pi/2$

Figure 10 shows the effect of additional inclusions when inclusions are aligned at $\theta = 0$, i.e. along the line perpendicular to an applied load. When the coating is compliant (coatings 1 and 2), increasing the number of inclusions increases the maximum effective stress in the matrix. However, adding each additional inclusion has a smaller contribution to the stress. When the coating is optimum or stiffer there is almost no effect of additional inclusions on σ^{m}_{eff}.

Figure 11 illustrates the effect of additional inclusions when the inclusions are aligned along the line of the applied load. When the elastic modulus of the coating is higher or equal to that of the matrix, i.e. $E^c/E^m \geqslant 1$, then the addition of inclusions increases the effective stress in the matrix but each additional inclusion has a smaller influence on stress. For the cases of coatings 2 or 3 (the optimum coating)

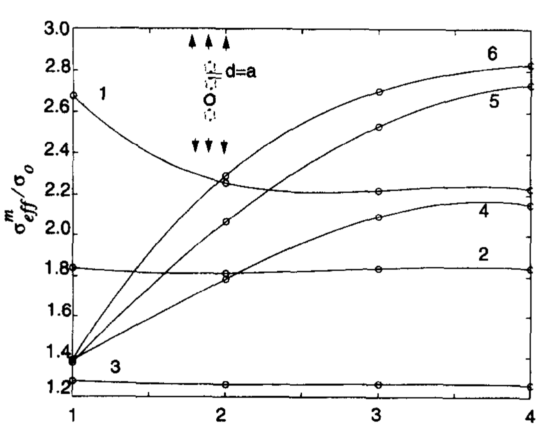

Fig. 11. Effect of number of inclusions on $\sigma^{m}_{eff}/\sigma_0$ for a uniaxial tension σ_0 in the vertical direction when $t = a/4$ and $\theta = \pi/2$.

Table 5. Maximum effective stress σ_{eff}/σ_0 in the matrix, inclusions, and coatings owing to two, three, and four inclusions separated by a constant distance $d = a$ for a uniaxial tension applied in the vertical direction for various coating cases ($t = a/4$)

Coating	$\sigma^{m}_{eff}/\sigma_0$	$\sigma^{c}_{eff}/\sigma_0$	$\sigma^{i}_{eff}/\sigma_0$	
1	3.94	0.012	0.048	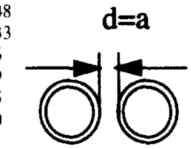
2	2.64	0.377	0.833	
3	1.26	1.13	1.36	
4	1.27	1.28	1.49	
5	1.32	1.35	1.75	
6	1.32	3.01	1.40	
1	2.26	0.012	0.036	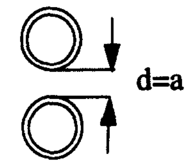
2	1.82	0.732	0.726	
3	1.26	1.14	1.36	
4	1.74	1.70	1.70	
5	2.07	2.49	1.94	
6	2.19	4.50	1.74	
1	3.68	0.011	0.021	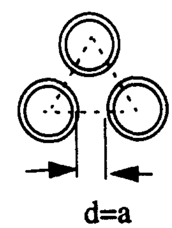
2	2.10	0.742	0.883	
3	1.28	1.13	1.27	
4	1.40	1.45	1.59	
5	1.59	1.68	1.79	
6	1.63	3.24	1.64	
1	3.82	0.041	0.053	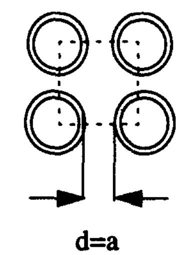
2	2.54	0.784	0.915	
3	1.28	1.16	1.27	
4	1.67	1.62	1.65	
5	1.98	1.93	1.90	
6	1.96	4.45	1.72	

there is no contribution to stresses when more inclusions are added. This tendency is reversed when the coating is very compliant (coating 1) and there is even a decrease in σ^{m}_{eff} as more inclusions are added.

Effect of Other Arrangements

In Table 5 we compare the maximum effective stress σ_{eff}, due to three and four inclusions in a triangular or square configuration and separated by a constant distance $d = a$, to the case of two inclusions separated by the same distance and subjected to the same uniaxial loading in the vertical direction. For the four inclusion case the effective stress in the matrix σ^{m}_{eff} between any two inclusions is more than σ^{m}_{eff} between two isolated inclusions inclined along the optimum path but slightly less than σ^{m}_{eff} between two inclusions aligned along the critical path. The opposite behavior was observed for stresses in the coating and the inclusions. Also, three inclusions give a lower stress in all three components than the four inclusion configuration. This is due to the angle of inclination of inclusions which is more critical in the square case. Note that for the optimum coating case the stress is almost unchanged for all four configurations and all three components.

4.3.4. Other factors (plane strain case, other volume fractions). All our numerical examples are for the plane stress case. We choose this case for experimental simplicity, as discussed in the Introduction. We compared plane stress and plane strain stress results and found that plane stress gave higher stresses for both single and multi-inclusion geometries [46]. We do not include these results here due to space limitation.

We also considered the higher volume fraction ($f = 46\%$) case. In this situation the magnitudes of the maximum stress were on average higher than for $f = 23\%$ owing to a higher probability of closer distances between inclusions.

5. FINAL REMARKS

In this paper we studied the model composite material for experimental simplicity; thick coatings were chosen for both experimental and numerical convenience. The material mismatch, considered here, is most closely applicable to polymer matrix composites due to a high inclusion–matrix moduli ratio. A similar approach can be used to study metal–matrix and ceramic–matrix composites. However, the focus of this research was not to study a specific composite system but to understand the complex phenomena influencing local stresses in matrix–inclusion composite materials.

Finally, we neglected the effect of thermal residual stresses. This subject has been investigated separately [46]. We isolated mechanical and thermal factors in order to gain a more fundamental understanding of the elastic events.

6. CONCLUSIONS

In this paper we studied the joint influence of the inclusion–matrix interface and the geometric arrangement on local stress fields of the model composite having circular copper inclusions (with thick coatings) in a photoelastic matrix. We found that both of these factors significantly contribute to the local stress fields. A random arrangement of inclusions gives rise to higher stress concentrations in the matrix than periodic ones owing to a localization of stresses. The compliant interface cases gives much higher stress concentrations in the matrix although inclusions are stiffer. This is due to the fact that there is almost no load transfer across the interface and thus the matrix carried the load. Also, the compliant interface cases give a much higher scatter in the magnitudes of maximum local stresses than stiffer coating cases. In addition, we considered simpler geometries involving one, two, and several inclusions in order to gain a fundamental understanding of stresses in a multi-inclusion environment. We conducted a parametric study and investigated how the stresses depend on the distance between the two closest inclusions, their angle of inclination with respect to the applied loading, and the presence of additional inclusions. A more complete study of the effects of a random arrangement of inclusions requires a stochastic analysis, which will be the subject of future investigation.

Acknowledgements—We would like to thank Professors G. Cloud, A. Lee, M. Ostoja-Starzewski, M. F. Thorpe, and Dr L. C. Davis for helpful discussions on this project. We gratefully acknowledge the financial support of the Research Excellence Fund from the State of Michigan, the NSF grant No. MSS 9402285, and the NSF Center for Low-Cost, High-Speed Polymer Composites Processing.

REFERENCES

1. Eshelby, J. D., *Proc. R. Soc.*, 1957, **A241,** 376.
2. Mura, T., *Micromechanics of Defects in Solids*, 2nd edn. Martinus Nijhoff, Dordrecht, 1987.
3. Mori, T. and Wakashima, K., in *Micromechanics and Inhomogeneity, the Mura Anniversary Volume*, ed. G. J. Weng, M. Taya and H. Abe. Springer, New York, 1990, p. 269.
4. Benveniste, Y., Dvorak, G. J. and Chen, T., *Mech. Mater.*, 1989, **7,** 305.
5. Tong, Y. and Jasiuk I., in *Proc. American Society for Composites*. 5th Technical Conference, Technomic, Lancaster, PA, 1990, p. 117.
6. Robertson, D. D. and Mall, S., *J. Compos. Technol. Res.*, 1992, **14,** 3.
7. Bigelow, C. A., *J. Comp. Technol. Res.*, 1992, **14,** 211.
8. Li, D. S. and Wisnom, M. R., *Comp. Sci. & Technol.*, 1994, **51,** 545.
9. Zhu, H. and Achenbach, J. D., *Mech. Mater.*, 1991, **11,** 347.
10. Gosz, M., Moran, B. and Achenbach, J. D., *Int. J. Damage Mech.*, 1994, **3,** 357.
11. Sorensen, F. and Talreja, R., *Mech. Mater.*, 1993, **16,** 351.
12. Bohm, J., Rammerstorfer, F. G., Fisher, F. D. and Siegmund, T., *J. Engng Mater. Technol.*, 1994, **116,** 268.
13. Ohno, N. and Hutchinson, J. W., *J. Mech. Phys. Solids*, 1984, **32,** 63.
14. Basista, M. and Krajcinovic, D., *Comp. Engng*, 1991, **1,** 103.
15. Becker, R. and Smelser, R. E., *J. Mech. Phys. Solids*, 1994, **42,** 773.
16. Pyrz, R. and Bochenek, B., *Sci. Engng Comp. Mater.*, 1994, **3,** 95.
17. Pyrz, R., *Comp. Sci. Technol.*, 1994, **50,** 197.
18. Ostoja-Starzewski, M., Sheng, P. and Jasiuk, I., *J. Engng Mater. Technol.*, 1994, **116,** 384.
19. Brockenbrough, J. R., Suresh, S. and Wienecke, H. A., *Acta metall. mater.*, 1991, **39,** 735.
20. Day, A. R., Snyder, K. A., Garboczi, E. J. and Thorpe, M. F., *J. Mech. Phys. Solids*, 1992, **40,** 1031.
21. Snyder, K. A., Garboczi, E. J. and Day, A. R., *J. appl. Phys.*, 1992, **72,** 5948.
22. Davis, L. C., Hass, K., Chen, J. and Thorpe, M. F., *Appl. Mech. Rev.*, 1994, **47**(2), S5.
23. Chen, J., Thorpe, M. F. and Davis, L. C., *J. appl. Phys.*, 1995, **77,** 4349.
24. Ghosh, S. and Mukhopadhyay, S., *Comput. Methods Appl. Mech. Engng*, 1993, **104,** 211.
25. Zhang, J. and Katsube, N., *Finite Elements in Analysis and Design*, 1995, **19,** 45.
26. Gong, S. X. and Meguid, S. A., *Acta mech.*, 1993, **99,** 49.
27. Honein, E., Honein, T. and Herrmann, G., *J. Engng Mater. Technol.*, 1994, **16,** 298.
28. Kouris, D. and Marshall, D., *J. Engng Mater. Technol.*, 1994, **116,** 319.

29. Kouris, D. and Tsuchida, E., *Mech. Mater.*, 1991, **12,** 131.
30. Kouris, D., *J. appl. Mech.*, 1993, **60,** 203.
31. Daniel, I. M. and Durelli, A. J., *Expl Mech.*, 1962, **2,** 240.
32. Parks, V. J. and Durelli, A. J., *J. appl. Mech.*, 1965, **32,** 504.
33. Durelli, A. J., Parks, V. J., Feng, H. and Chiang, F., in *Mechanics of Composite Materials*, ed. F. W. Wendt, H. Liebowitz and N. Perrone. Pergamon Press, Oxford, 1967, p. 265.
34. Marloff, R. H. and Daniel, I. M., *Expl Mech.*, 1969, **9,** 156.
35. Javornicky, J., *Exp. Stress. Anal.*, 1970, 39.
36. Drzal, L. T., *Adv. Polym. Sci.*, 1985, **75,** 1.
37. Broutman L. J. and Agarwal, B. D., *Polym. Engng Sci.*, 1974, **14,** 581.
38. Pagano, N. J., *Comp. Sci. Technol.* 1988, **31,** 273.
39. Nimmer, R. P., Bankert, R. J., Russell, E. S., Smith G. A. and Wright, P. K., *J. Comp. Technol. Res.*, 1991, **13,** 3.
40. Arnold, S. and Wilt, T., *Comp. Interfaces*, 1993, **1,** 381.
41. Kerans, R. J., Hay, R. S., Pagano, N. J. and Parthasarathy, T. A., *Ceram. Bull.*, 1989, **68,** 429.
42. Hughes, J. D. H., *Comp. Sci. Technol.*, 1991, **41,** 13.
43. Wright, W., *Comp. Polymer.*, 1990, **3,** 360.
44. Al-Ostaz, A. and Jasiuk, I., in *Durability of Composite Materials*, MD-Vol. 51, ed. R. C. Wetherhold, ASME, New York, 1994, p. 207.
45. Al-Ostaz, A. and Jasiuk, I., in *Durability and Damage of Composite Materials*, Vol. 2, ed. N. Sottos *et al.* ASME, New York, 1995, p. 254.
46. Al-Ostaz, A. The influence of random arrangement and interface on elastic fields and fracture of model composite materials. Ph.D. dissertation, Michigan State University, 1996.
47. Timoshenko, S. P. and Goodier, J. N., *Theory of Elasticity*, 3rd edn. McGraw-Hill, New York, 1993.
48. Mendelson, A., *Plasticity: Theory and Application.* Krieger, Malambar, FL, 1968.
49. *ANSYS 5.1 User Manual.* Swanson Analysis Systems, Inc., Houston, 1995.
50. Dally, J. W. and Rilley, W. F., *Experimental Stress Analysis*, 3rd end. McGraw-Hill, New York, 1991.
51. Lee, M., Jasiuk, I. and Tsuchida, E., *J. appl. Mech.*, 1992, **59,** S57.
52. Carman, G. P., Averill, R. C., Reifsnider, K. L. and Reddy, J. N., *J. Comp. Mater.*, 1992, **27,** 589.
53. Duan, Z. P., Kiesler, R. and Herrmann, G., *J. Mech. Phys. Solids*, 1986, **43,** 539.
54. Zimmerman, R. W., *Mech. Res. Commun.*, 1988, **15,** 87.